Experimental and Numerical Study of Confined Coaxial Turbulent Jets

J. M. Khodadadi* and N. S. Vlachos†
University of Illinois at Urbana-Champaign, Urbana, Illinois

The turbulent mixing of a primary jet and its surrounding fluid in a pipe with inlet conditions that result in flow separation is studied. Detailed profiles of the axial mean and rms velocities have been measured with a laser Doppler anemometer. Measured spectra of axial velocity fluctuations show the presence of coherent structures. The performance of a two-equation turbulence model in conjunction with a finite-difference-based numerical prediction procedure was tested for selected previous experimental data. Computations using the presently measured inlet profiles were also performed, resulting in satisfactory agreement. It is concluded that numerical diffusion, streamline curvature, and the presence of coherent structures in the case of strong separation result in deteriorating agreement.

Nomenclature

a = radius ratio r_j/R
Ct = Craya-Curtet number
D = diameter of the mixing tube
k = turbulence kinetic energy
L = length of the mixing tube
P = pressure
r = radial coordinate
r_j = jet radius
R = radius of the mixing tube
Re = Reynolds number
St = Strouhal number, i.e., $f(2r_j)/U_{jm}$
u = fluctuating component of axial velocity
U = time-averaged axial velocity
v = fluctuating component of radial velocity
V = time-averaged radial velocity
V_{tot} = velocity magnitude $(U^2 + V^2)^{0.5}$
z = axial coordinate
ϵ = rate of dissipation of turbulence energy
μ = dynamic viscosity of the fluid
μ_f = false or numerical viscosity
μ_t = turbulent or eddy viscosity
ν = kinematic viscosity of the fluid
ρ = fluid density
$\langle \cdots \rangle$ = time-averaged value

Subscripts

1,2 = primary and secondary streams
j = primary stream
m = mean
s = secondary stream
t = turbulent

Presented as Paper 87-1380 at the 19th AIAA Fluid Dynamics, Plasma Dynamics and Lasers Conference, Honolulu, HI, June 8-10, 1987; received Dec. 21, 1987; revision received May 5, 1988.

*Currently Assistant Professor, Department of Mechanical Engineering, Auburn University. Member AIAA.

†Assistant Professor, Department of Mechanical and Industrial Engineering; currently Senior Manager, Engineering and Consulting Division, CHAM of North America, Inc., Huntsville, AL. Member AIAA.

I. Introduction

THE mixing of nonreacting and reacting fluids is encountered in many practical engineering applications. The simplest example of confined mixing of two fluid streams is that of a turbulent jet issuing into a circular pipe, as shown in Fig. 1. The primary fluid with a mean velocity U_1 entrains and mixes with the secondary fluid of mean velocity U_2. This flow entails many regimes of interest, i.e., potential cores, boundary-layer development in adverse pressure gradient, regions of similar velocity profiles, possible separation regions, etc. The presence of large-scale structures and their effect on the turbulence transport introduce an additional challenge. The major objective of the present work was to obtain detailed measurements, particularly in the initial mixing region, in order to study the physical phenomena and the existence of organized flow structures. The measurements were then compared with predictions in order to assess a two-equation turbulence model as applied to confined mixing.

The following review of previous work is rather brief. More detailed information can be found in Khodadadi.[9] Becker et al.[2] measured mean velocity and concentration, using impact tubes and light-scattering techniques, respectively. They also introduced the Craya-Curtet number as a universal parameter for confined jet systems

$$Ct = \frac{U_m}{[(U_1^2 - U_2^2)a^2 + 0.5(U_2^2 - U_m^2)]^{1/2}} \tag{1}$$

where $U_m = (U_1 - U_2)\, a^2 + U_2$ is the mean velocity in the mixing tube. From a physical point of view, large or small values of Ct correspond to small or large excess inlet momentum, respectively. Becker et al.[2] suggested that the appearance of the recirculation is limited to $Ct < 0.85$. Barchilon and Curtet[1] measured mean velocities, variation of wall static pressure and size of the recirculation zone for water flow, and rms values of the axial velocity fluctuations for airflow. A comprehensive study was carried out by Razinsky and Brighton[17] using an impact tube and a hot-wire anemometer. They provided details of the structure of confined mixing with no separation and its transition to the fully developed state.

Suzuki et al.[18] reported a study of the turbulence structure and heat transfer in confined coaxial jets. They measured mean velocities, rms values of axial velocity fluctuations, and distribution of the Nusselt number. They observed that the maximum intensity of the near-wall turbulence occurred very close to the maximum heat-transfer position, which happened to be within the separation region and not at the reattachment

point. Kang and Suzuki[7] used the SIMPLE[16] procedure and the k-ϵ turbulence model of Launder and Spalding[14] to predict the extensive data of Razinsky and Brighton.[17] Kang and Suzuki[8] later reported heat-transfer predictions of separated flow in the entrance region of the mixing tube. The heat-transfer rate close to the inlet was affected by the prescribed inlet velocity distribution. However, no significant change in the augmented heat-transfer region further downstream was observed. Fairly good agreement was achieved between predicted and measured local Nusselt numbers.

Although both separating and nonseparating flows have been studied, the lack of reliable and detailed velocity measurements, particularly at the inlet plane, has limited the meaningful comparison of numerical predictions to experiments. In addition, definitive conclusions in regard to grid distribution, convergence characteristics, and numerical inaccuracies were not drawn. The present work addresses these deficiencies and provides detailed measurements for model testing.

II. Computational Details

The present work utilizes the SIMPLE procedure outlined by Patankar.[16] The advantages of this scheme over the "vorticity-stream function" formulations are the use of primitive variables, i.e., velocity components and pressure, and its easy extension to three-dimensional separating flows.

Time-Averaged Equations and Turbulence Model

The equations governing the present axisymmetric flow may be written in the following general form:

$$\frac{\partial}{\partial z}(\rho U\phi) + \frac{1}{r}\frac{\partial}{\partial r}(\rho r V\phi) = \frac{\partial}{\partial z}\left(\Gamma_\phi \frac{\partial \phi}{\partial z}\right) + \frac{1}{r}\frac{\partial}{\partial r}\left(\Gamma_\phi r \frac{\partial \phi}{\partial r}\right) + S^\phi \tag{2}$$

where U and V are the time-averaged velocities in the axial and radial directions, respectively. The variable ϕ represents various time-averaged quantities, i.e., mean velocities, turbulence kinetic energy, etc. The transport equations and the constants of the k-ϵ turbulence model of Launder and Spalding[14] used for the present computations are summarized in Table 1. Four variations of the standard k-ϵ model which account for streamline curvature effects were considered.

1) Durst and Rastogi[5] suggested replacing the generation term G in the k-ϵ model by $S_c \cdot G$, where

$$S_c = 1.15\ \{1 - \exp[11.3(F - 0.18)]\}$$

$$F = \frac{V_{\text{tot}}}{R_c \cdot (\partial V_{\text{tot}}/\partial R_c)} \tag{3}$$

The curvature radius is

$$\frac{1}{R_c} = \frac{UV\left(\frac{\partial V}{\partial r} - \frac{\partial U}{\partial z}\right) + U^2\frac{\partial V}{\partial z} - V^2\frac{\partial U}{\partial r}}{(U^2 + V^2)^{1.5}} \tag{4}$$

S_c was set to zero for $F \geq 0.18$.

2) Leschziner and Rodi[15] incorporated the effects of streamline curvature on C_μ in the form

$$C_\mu = \max\left\{0.025, \frac{0.09}{\left[1 + 0.57\frac{k^2}{\epsilon^2}\left(\frac{\partial V_{\text{tot}}}{\partial n} + \frac{V_{\text{tot}}}{R_c}\right)\frac{V_{\text{tot}}}{R_c}\right]}\right\} \tag{5}$$

3) Hanjalic and Launder[6] recommended the addition of an extra term to the transport equation for ϵ. This term emphasizes the role of irrotational deformations in promoting energy transfer across the spectrum by modifying the production term $(\epsilon/k)C_1 G$ to read

$$(\epsilon/k)\ [C_1' G - C_1'' \mu_t S_{ns}^2] \tag{6}$$

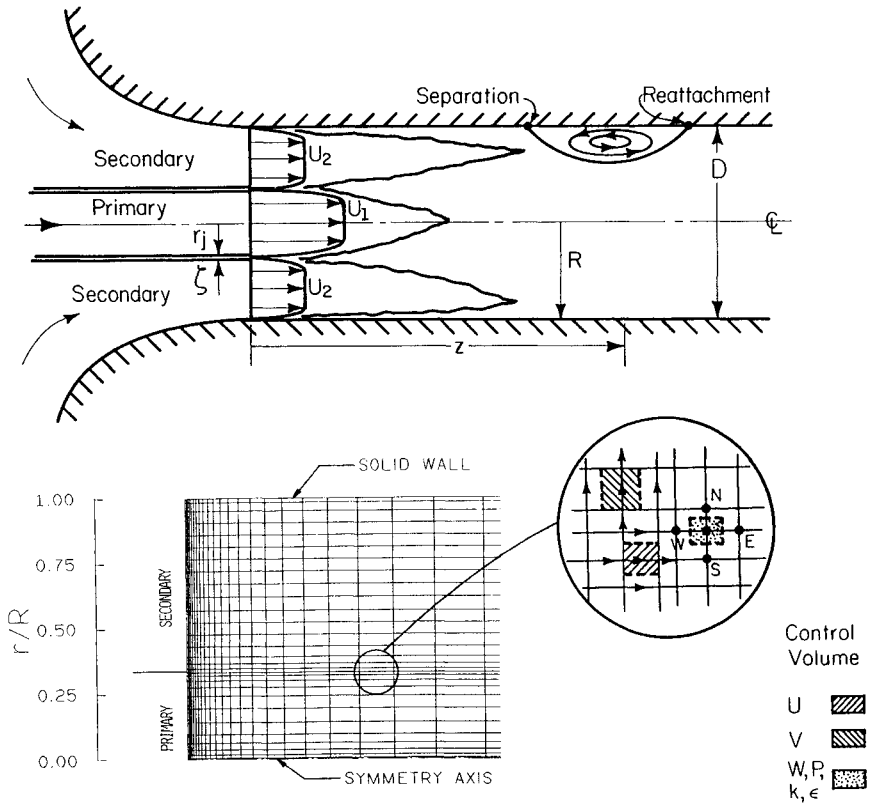

a) Confined coaxial jet flow

b) Computational grid

Fig. 1 Schematic of confined jet mixing and computational grid.

Table 1 Transport equations and turbulence model constants

	ϕ	Γ_ϕ	S^ϕ
Continuity	1	0	0
Axial momentum	U	μ_{eff}	$\frac{\partial}{\partial z}\left(\mu_{\text{eff}}\frac{\partial U}{\partial z}\right)+\frac{1}{r}\frac{\partial}{\partial r}\left(r\mu_{\text{eff}}\frac{\partial V}{\partial z}\right)-\frac{\partial P}{\partial z}$
Radial momentum	V	μ_{eff}	$\frac{\partial}{\partial z}\left(\mu_{\text{eff}}\frac{\partial U}{\partial r}\right)+\frac{1}{r}\frac{\partial}{\partial r}\left(r\mu_{\text{eff}}\frac{\partial V}{\partial r}\right)-\frac{\partial P}{\partial r}-2\mu_{\text{eff}}\frac{V}{r^2}$
Kinetic energy	k	$\frac{\mu_{\text{eff}}}{\sigma_k}$	$G-\rho\epsilon$
Dissipation rate	ϵ	$\frac{\mu_{\text{eff}}}{\sigma_\epsilon}$	$\frac{\epsilon}{k}(C_1G-C_2\rho\epsilon)$

$$G=\mu_{\text{eff}}\left\{2\left[\left(\frac{\partial U}{\partial z}\right)^2+\left(\frac{\partial V}{\partial r}\right)^2+\left(\frac{V}{r}\right)^2\right]+\left(\frac{\partial U}{\partial r}+\frac{\partial V}{\partial z}\right)^2\right\}$$

$$\mu_{\text{eff}}=\mu+\mu_t, \qquad \mu_t=C_\mu\rho k^2/\epsilon$$

$$C_\mu=0.09, \quad C_1=1.44, \quad C_2=1.92, \quad \sigma_k=1.0, \quad \sigma_\epsilon=1.22$$

where $C_1'=2.24$, and $C_1''=0.8$. The streamwise shear strain S_{ns} is calculated as suggested by Leschziner and Rodi.[15]

4) The last modification investigated is simply the combination of those proposed by Leschziner and Rodi[15] and Hanjalic and Launder.[6]

Boundary Conditions and Solution Procedure

At the outlet, the flow was assumed to be fully developed; i.e., the axial gradients of all variables were set to zero. The radial velocity and the normal gradient of other variables were set to zero at the symmetry axis. The standard wall function outlined by Launder and Spalding[14] was used for the next-to-the-wall grid points, while no attempt was made to account for adverse pressure gradients. The inlet conditions will be presented in Sec. IV, along with the numerical results.

A nonuniform grid shown in Fig. 1 was used with finer spacing in the regions of large spatial gradients, i.e., the initial mixing region in the tube. Staggered control volumes were used for the axial and radial velocity components. All other quantities of interest were computed at the grid points. The finite-difference forms of the time-averaged equations were obtained by adopting a semi-integral approach to discretize the equations over each control volume of the computational grid.[16] A hybrid difference scheme that combines central and upwind differencing was used. The line-by-line method was employed to obtain converged solutions iteratively. Underrelaxation factors were used to promote stability with values of 0.3, 0.2, 0.8, and 0.8 for U, V, k, and ϵ, respectively. The turbulent viscosity field was underrelaxed with a value of 0.3, whereas no relaxation was applied to the pressure correction field. The iterations were terminated when the sum of the absolute residuals (normalized, e.g., by the inlet mass flow rate, etc.) was less than 10^{-4}.

To assess the extent of the numerical error, the numerical diffusion coefficient suggested by de Vahl Davis and Mallinson[3]

$$\mu_f=\frac{\rho V_{\text{tot}}\Delta r\Delta z\sin 2\psi}{4(\Delta r\sin^3\psi+\Delta z\cos^3\psi)} \tag{7}$$

was evaluated for the entire flowfield. In this equation, Δr and Δz are the grid spacings in the radial and axial directions, respectively, and ψ is the angle made by the local velocity vector with the axial direction. The appropriateness of this analysis for laminar flow in a 90-deg bifurcation has been discussed by Khodadadi et al.[10] From the physical viewpoint, the numerical diffusion coefficient is a measure of the deviation from the true effective viscosity.

III. Experimental Details

A schematic diagram of the flow test section is shown in Fig. 2. A regulated airflow was allowed to develop in a 1-in. pipe for 48 diam before it reached the primary nozzle with a contraction area ratio of 4:1 over a 2-in. distance. The secondary stream was induced by the momentum of the primary jet from the atmosphere through a wooden bellmouth of 7.37 area ratio. Two plexiglas mixing tubes with 4.25- and 6.5-in. diam were used. The nozzle wall thickness was kept to a minimum at 0.1 in., and the primary pipe was centered in the tubes with an accuracy of 0.05 in.

The one-channel, dual-beam, forward-scatter laser Doppler anemometer (LDA) that was designed and constructed during the present study is also shown in Fig. 2. A 15-mW He-Ne laser (Spectra-Physics, 124B) was focused on a diffraction grating (TPD, type R-H) to obtain two first-order beams of equal intensity, which were focused by lenses to form the optical control volume. A light-collecting lens and a photomultiplier (Hamamatsu R1104) with a 0.2-mm-diam pinhole were used to obtain the Doppler signal. The LDA system was bolted to an XY milling table, which was placed on a heavy,

Table 2 Characteristics of the laser Doppler anemometer

15-mW He-Ne laser wavelength	632.8 nm
Laser beam diameter	1.1 mm
Number of grating line pairs	8192
First-order angle	3.15 deg
Grating speed of rotation	3000 rpm
Frequency shift	819.2 kHz
Focal length of lenses:	
Focusing (f_1)	165 mm
Collimating (f_2)	200 mm
Imaging (f_3)	200 mm
Half-angle of intersection	3.12 deg
Fringe separation (d_f)	5.813 μm
Dimensions of measuring volume:	
b_x	121 μm
b_y	2.22 mm
Number of stationary fringes	21
Anemometer transfer constant	5.813 (m/s)/MHz

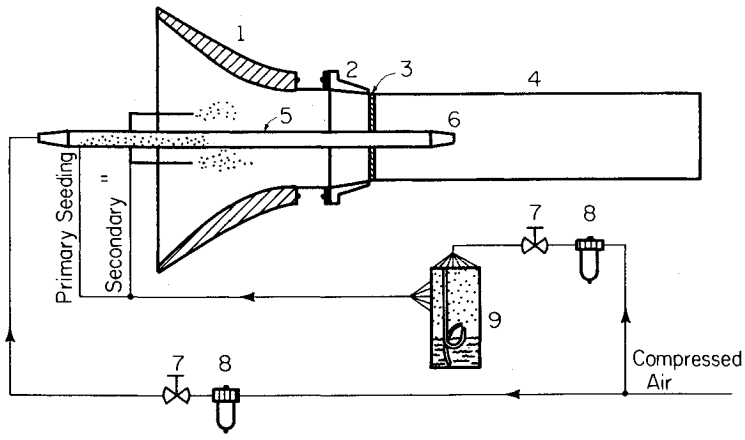

1 Contraction
2 Adaptor
3 Grid
4 Plexiglass Tube
5 Primary Pipe
6 Nozzle
7 Pressure Regulator
8 Filter
9 Atomizers

a) Flow test section

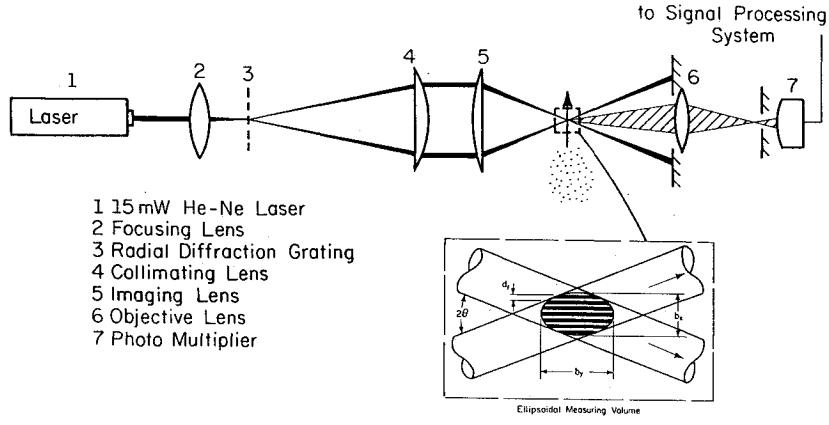

b) Laser Doppler anemometer

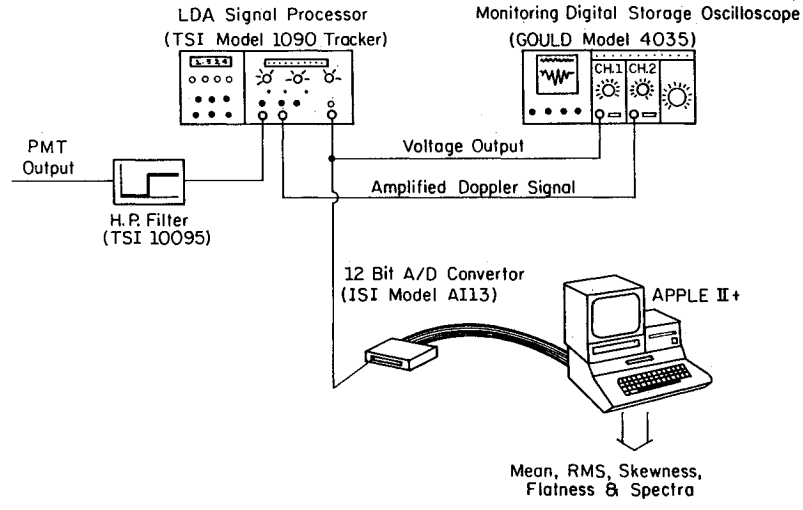

c) Signal processing system

Fig. 2 Schematic of the flow and diagnostic apparatus.

upright table that allowed vertical adjustments to be made. Seeding particles were produced by a series of silicone oil (Dow 200) atomizers.

The beam frequency shift required for backflow measurements was obtained from the frequency difference between the beams when rotating the diffraction grating. The velocity-frequency response of the LDA is given by $V = (f_D - f_s)\, d_f$, where f_D is the frequency of the Doppler signal, f_s the frequency shift, and d_f the interference fringe spacing. The frequency shift is calculated from $f_s = 2nN$, where n is the number of the diffraction grating line pairs and N its rotational speed. The fringe spacing is given by $d_f = \lambda/(2 \sin\theta)$, where λ is the beam wavelength and θ the half-angle of the intersecting beams. The main operating characteristics of the LDA unit are summarized in Table 2.

A schematic diagram of the signal processing equipment is also shown in Fig. 2. The Doppler signal was directed to a frequency tracker (TSI, 1090). The tracker voltage output representing the instantaneous velocity and the amplified Doppler signal were monitored on a digital storage oscilloscope (Gould, 4035). The tracker output was then digitized by a 12-bit A/D converter (IS, AI13), and statistical signal processing was performed on an Apple II+, using machine language. The statistical analysis was based on 16,000 samples/point, requiring less than 1 min of processing time.

The first measuring station was very close to the primary nozzle at $z \approx 0.03$ in. This station, where only the primary stream could be measured, was designated as the $z/R = 0$ station. The first stations where the entire diameter of the mixing tube could be accessed for measurements were located

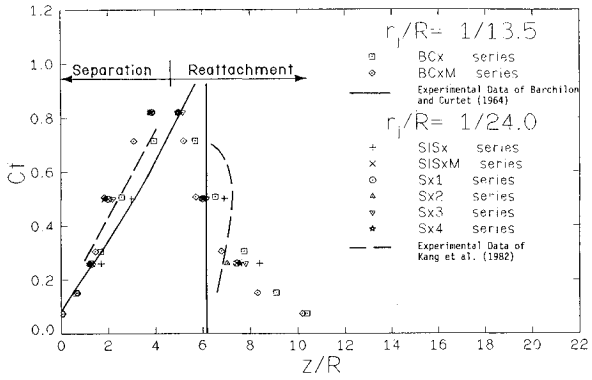

Fig. 3 Locations of separation and reattachment points.

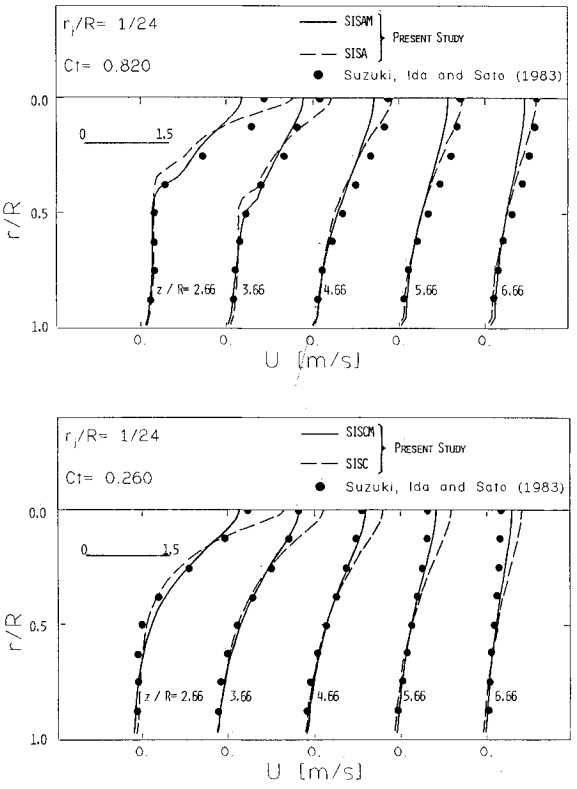

Fig. 4 Comparison of mean axial velocity profiles.

at $z/R \approx 0.05$ and 0.06 for the small and large tubes, respectively. Uncertainty estimates were performed following the technique suggested by Kline and McClintock.[12] It was estimated that the maximum uncertainties in the measured values of U and $<u^2>$ were 2 and 5%, respectively.

IV. Results and Discussion

The turbulence model was tested for developing pipe flow (limiting case of $Ct \to \infty$) and the nonseparating confined jet flow reported by Razinsky and Brighton.[17] The results were in good agreement with experiment and can be found in Khodadadi[9] and Khodadadi and Vlachos.[11]

Predictions of Previously Measured Flows

The work of Barchilon and Curtet[1] was primarily a flow visualization study and was selected for comparison of the overall flow features. The predicted locations of the separation and reattachment points are presented in Fig. 3. The separation point is predicted well, whereas the reattachment point is observed to move downstream with decreasing Ct.

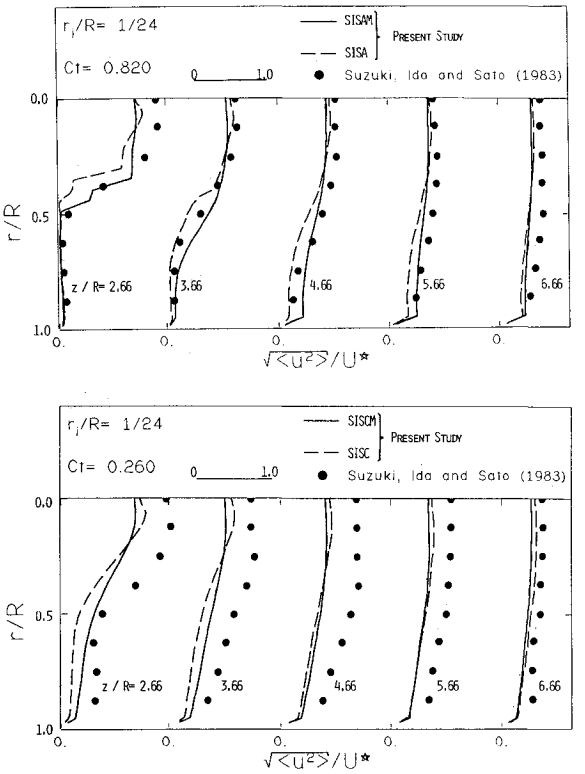

Fig. 5 Comparison of rms velocity fluctuations.

Experimental findings[1] suggest that the reattachment point should remain fixed at $z/R = 6$. Further details, e.g., centerline velocity decay and wall pressure distribution, can be found in Khodadadi.[9]

Table 3 summarizes the computational details for the flow conditions of Suzuki, Ida, and Sato[18] (SIS cases). In the absence of detailed entrance conditions, inlet profiles similar to the work of Kang and Suzuki[7] were utilized. Grid independence tests[9] were performed which led to the adoption of a 35×30 grid for final production runs. The SISxM series of computations were based on a 35×30 axially expanding grid. Another set of predictions (the SISx series) which used a 30×30 axially uniform grid similar to that of Kang and Suzuki[7] with the radial grid arrangement of SISxM series was also obtained in order to assess the effect of grid spacing.

The impact of the grid can be seen in Fig. 4, where measured mean axial velocities are compared to the predictions. The solid curves represent the SISxM, and the dashed lines correspond to the SISx series of computations. The SISx overpredict both the experimental data and the SISxM cases along the centerline. The comparison inside the reverse flow region ($Ct = 0.26$) is good. The rms profiles of the axial velocity fluctuations are presented in Fig. 5. The turbulence levels of the SISxM series are higher than the SISx predictions for the range of $0.4 < r/R < 1.0$, whereas for $r/R < 0.4$, the SISx cases generally predict turbulence levels higher than their SISxM counterparts. The comparison with the measurements ranges from poor (all of the stations for $Ct = 0.26$) to very good (profiles at $z/R = 2.66$ and 3.66 for $Ct = 0.82$). At the stations farther downstream, the mismatching of the measurements and the predictions reappears. The consistent underprediction for the last three stations can be viewed in light of the streamline curvature effects in this zone. The recirculation region redirects the streamlines, thus causing excessive numerical diffusion. Another contributing factor may be the isotropic nature of the k-ϵ model, which cannot handle reverse flows appropriately.

Figure 6 depicts the contours of the numerical diffusion coefficient for $Ct = 0.82$, 0.50, and 0.26. The separation points are also identified in this figure. The zones of excessive numerical diffusion are concentrated at the shear layer and extend for about 3 pipe radii from the inlet plane.

Examination of the Turbulence Model Variations

The turbulence model modifications discussed in Sec. II were applied only to the flow conditions of Suzuki et al.[18] The computational details are similar to the SIS*xM* series and are summarized in Table 3. The predicted separation and reattachment points for the S*x*1, S*x*2, S*x*3, and S*x*4 series corresponding to the four model modifications are identified in Fig. 3, along with those for the SIS*x* and SIS*xM* series. An attempt was made to examine the performance of the four turbulence model modifications against the standard k-ϵ model by comparing the results of the cases in Table 3 to the results of the SIS*xM* series presented in Figs. 4 and 5. None of these comparisons will be presented here, since no significant deviations in both the mean and fluctuating velocities were observed.

Predictions of Presently Measured Flows

The flow conditions for the present experiments are summarized in Table 4. For reasons of brevity, selected results are presented, compared, and discussed here. The interested reader is referred to Khodadadi[9] for further details. The present experimental results can be viewed as an attractive source for verification of numerical predictions for this class of flows. This is due mainly to the measurement of detailed inlet boundary conditions which have not been obtained by previous investigators. Three of the six cases summarized in Table 4 were selected for comparison purposes with the computational details indicated in Table 4. The confined jet (CJ*xx*) series of computations is based on the expanding grid used for the SIS*xM* cases. The measured mean velocity profiles at $z/R \approx 0.05$ and 0.06 were used as inlet conditions for the CJ*Ax* and CJ*Bx* series, respectively. The other inlet conditions were

$$k = (3/2)\langle u^2 \rangle, \qquad \epsilon = C_\mu k^{1.5}/l$$

$$l_1 = C_\mu^{0.25}(0.09\, r_j), \qquad l_2 = C_\mu^{0.25}[0.09(R - r_j)]$$

To determine the asymmetry of the measurements, the profiles are presented for the entire diameter of the mixing tube. The solid lines represent the predicted profiles, whereas the circles and squares correspond to the measured values. The mean velocity profiles for the case CJ*A*2 shown in Fig. 7 are predicted very well at all of the stations except $z/R = 4$ and 6, which are located in the region where adverse pressure gradient is present. In particular, the profile at the $z/R = 4$ station resembles a turbulent boundary layer approaching separation. Even though the Ct number is very close to the range where separation could be observed, LDA measurements near the wall between the $z/R = 4$ and 5 stations did not uncover any reverse flow. The utilization of the "law of the wall," which is based on zero or favorable pressure gradient, might contribute to the mismatchings of the profiles at $z/R = 4$ and 6. The profiles downstream of the $z/R = 4$ station all tend to decay toward the wall, and finally, at 16 radii, a plug profile is established and the agreement of the measured and predicted mean velocity profiles is excellent.

At the first station, where the entire diameter of the tube can be accessed for measurements, i.e., $z/R = 0.05$, the rms values in the core of the primary jet and in the secondary stream are of the same order of magnitude as shown in Fig. 8.

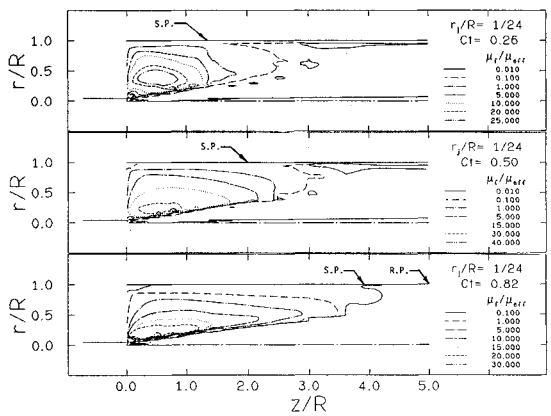

Fig. 6 Numerical diffusion coefficient.

Table 3 Computational details for flows of Suzuki et al.[18]

Case	Ct	Iterations	L/D	R/r_j
SIS*AM*	0.82	2419	12.5	24
SIS*BM*	0.50	2503	12.5	24
SIS*CM*	0.26	2694	12.5	24
			Modification	
S*A*1	0.82	1328		
S*B*1	0.50	1454	Durst and Rastogi[5]	
S*C*1	0.26	1582		
S*A*2	0.82	1466		
S*B*2	0.50	1371	Leschziner and	
S*C*2	0.26	1753	Rodi[15]	
S*A*3	0.82	1526		
S*B*3	0.50	1584	Hanjalic and	
S*C*3	0.26	1726	Launder[6]	
S*A*4	0.82	1444		
S*B*4	0.50	1565	Refs. 6 and 15	
S*C*4	0.26	1767		

Table 4 Details of the present measurements and computations

		Experiments				Computations		
Mixing tube, in.	R/r_j	U_{jm}, m/s	U_{sm}, m/s	$Re = U_m D/\nu$	Ct	Case	L/D	Iterations
4¼	8.5	5.0	1.1	6.7×10^3	2.17			
	8.5	28.3	2.3	1.7×10^4	0.82			
	8.5	62.2	5.1	4.2×10^4	0.84	CJ*A*2	12.5	2348
6½	13	5.0	0.4	4.5×10^3	1.18			
	13	28.3	1.2	1.3×10^4	0.66	CJ*B*1	12.5	2278
	13	62.2	2.6	3.2×10^4	0.64	CJ*B*2	12.5	2499

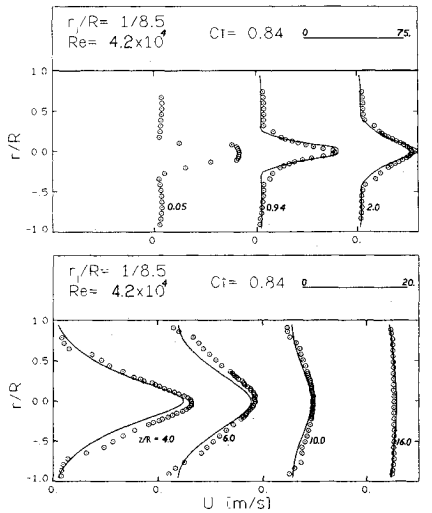

Fig. 7 Comparison of mean velocity profiles (CJ*A*2 series).

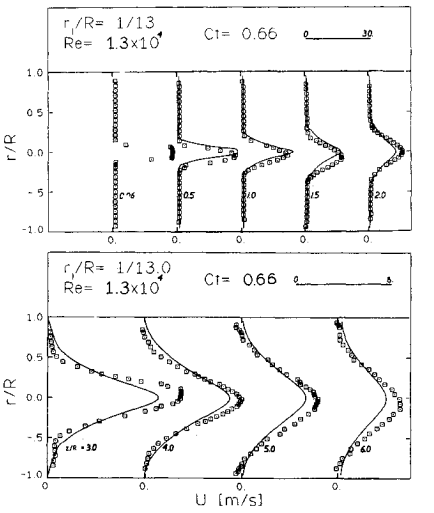

Fig. 9 Comparison of mean velocity profiles (CJ*B*1 series).

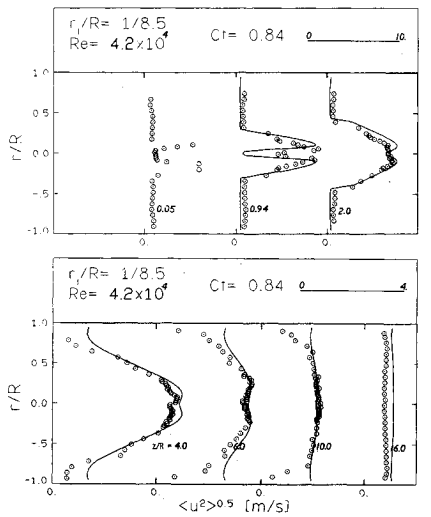

Fig. 8 Comparison of rms velocity profiles (CJ*A*2 series).

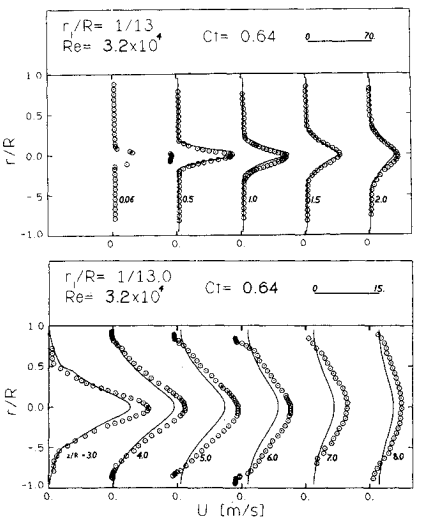

Fig. 10 Comparison of mean velocity profiles (CJ*B*2 series).

This indicates that the turbulence intensity of the secondary stream is much higher than that of the primary jet. The rms values of the secondary stream are not indicative of the fully developed state for annular flow because of the short distance between the contraction and the initiation of mixing. The large rms values at the interface of the primary and secondary streams are further enhanced at the downstream stations. These sites of intense turbulence activity lie in the shear layer, where entrainment and possible vortex shedding take place. The turbulence generated at the shear layer diffuses toward the core of the primary stream and, coupled with the decay of the primary jet, gives rise to monotonic increase of the turbulence intensity along the centerline. The turbulence produced in the initial mixing region is dissipated after the $z/R = 4$ station, and at the last measured station ($z/R = 16$) a plug profile is observed. The predicted rms profiles show satisfactory agreement with the measurements at the $z/R = 0.94$, 2, and 16 stations. The rest of the profiles at the $z/R = 4$, 6, and 10 stations exhibit only qualitative agreement near the wall. In general, the predicted turbulence levels for $r/R > 0.6$ are higher than the measurements for the stations located in the zone with adverse pressure gradient.

The measured mean velocity profiles are compared to the numerical results of the CJ*B*1 and CJ*B*2 cases in Figs. 9 and 10, respectively. Close examination of the mean velocity profiles in reverse flow regions reveals the asymmetric nature of the recirculation zone. The measured mean velocity profiles for the first two pipe radii are in excellent agreement with the numerical predictions. The developing velocity profiles in the mixing tube tend toward the profiles characteristic of boundary layers approaching separation ($z/R = 3$ station). The three profiles ($z/R = 4$, 5, and 6) were obtained at stations where a separation region was expected and the zone of reversed flow is clearly observed. The separation zone was found to extend from about 3.8–6.2 radii using next-to-the-wall LDA measurements, which is in accordance with observations by Barchilon and Curtet.[1] The radial positions at which the axial velocity is zero for the three profiles at the $z/R = 4$, 5, and 6 stations were found to be in good agreement with measurements of Suzuki et al.[18] and Becker et al.[2] The separation regions were strongly unsteady with intense fluctuations in spite of a small negative average velocity. The numerical predictions indicate a much smaller separation zone. Specifically, at the $z/R = 5$ and 6 stations, the numerical predictions show no reverse flow, whereas the measurements indicate its existence. The underestimation of the size of the separation zone with the k-ϵ model has been extensively reported for flow over backsteps and annular jets.[15]

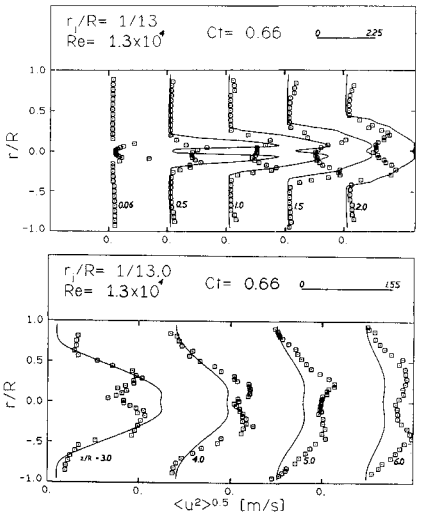

Fig. 11 Comparison of rms velocity profiles (CJ*B*1 series).

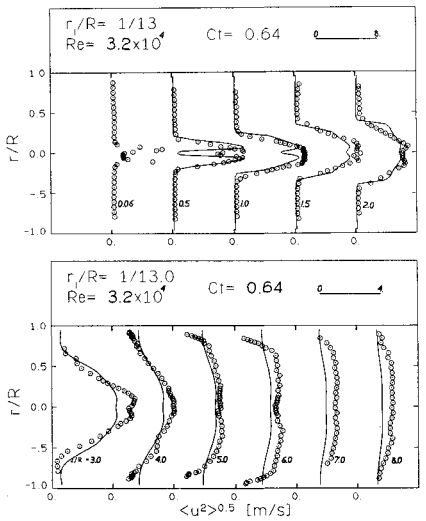

Fig. 12 Comparison of rms velocity profiles (CJ*B*2 series).

The rms profiles predicted by the CJ*B*1 series are shown in Fig. 11 and exhibit poor agreement with the measurements. At $z/R = 0.5$, 1.5, and 2, the model overpredicts the measured rms values in the vicinity of the symmetry axis. For the rest of the profiles at $z/R = 3$, 4, 5, and 6, only qualitative agreement is achieved between the measurements and predictions. The rms profiles of the CJ*B*2 series shown in Fig. 12 compare with the measurements much better than its CJ*B*1 counterpart discussed earlier, especially for the profiles in the first two pipe radii zone. At the downstream stations, beyond $z/R = 3$, the agreement deteriorates in the vicinity of the separation zone.

Spectra of the Centerline Axial Velocity

Spectral analysis is useful in determining the energy content and scales within a turbulent flowfield. High seeding-particle concentration resulted in an almost continuous signal of the frequency tracker velocity-analog output. The details of the software utilized during this phase of the study were outlined by Laker et al.,[13] and its application to LDA measurements in a confined round jet was reported by Vlachos.[19]

Traces of the instantaneous tracker voltage representing the axial velocity as observed on the digital storage oscilloscope are presented in Fig. 13. All traces were obtained along the centerline for a primary jet velocity of 5.0 m/s and show that the small-amplitude fluctuations are amplified selectively and proceed downstream to a more chaotic type of motion. The velocity traces are very similar to those of Vlachos[19] and Durao and Pita,[4] who reported LDA-based studies of coherent structures in the transitional region of confined jets and freejets, respectively.

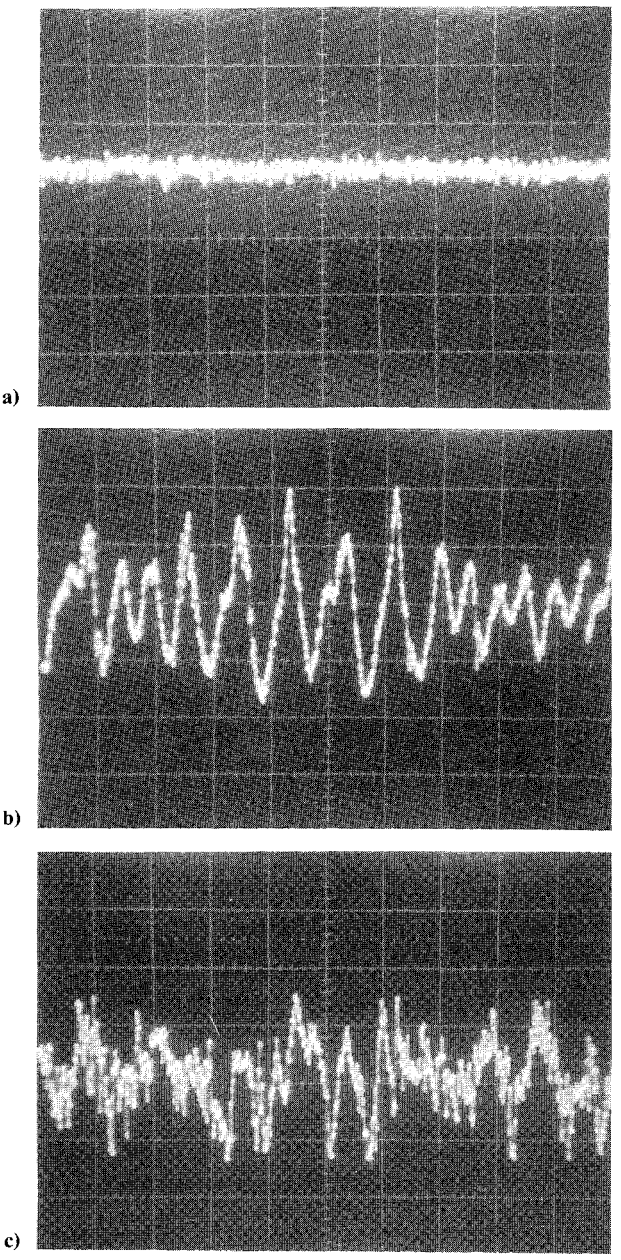

Fig. 13 Instantaneous centerline axial velocity for U_{jm} = 5.0 m/s: $z/(2r_j)$ = a) 0, b) 3, and c) 6. (Horizontal and vertical grids correspond to 10 m/s and 1.16 m/s, respectively.)

The frequency spectra of centerline axial velocity fluctuations obtained at stations $z/(2r_j) = 0.5$, 1, 2, and 4 are illustrated in Fig. 14. Arbitrary units are used for the vertical scales because only the relative power at each frequency is of interest. The dominance and coexistence of two frequencies at 69 and 200 Hz is evident at the first measurement station. At the two downstream stations $z/(2r_j) = 1$ and 2, the peak observed at 200 Hz becomes predominant, whereas the energy concentrated at 69 Hz decays. The Strouhal number at these locations is approximately 0.51. It is widely accepted that the Strouhal number is of the order of 0.3 for Reynolds numbers higher than 10^5 and increases with decreasing Reynolds number.

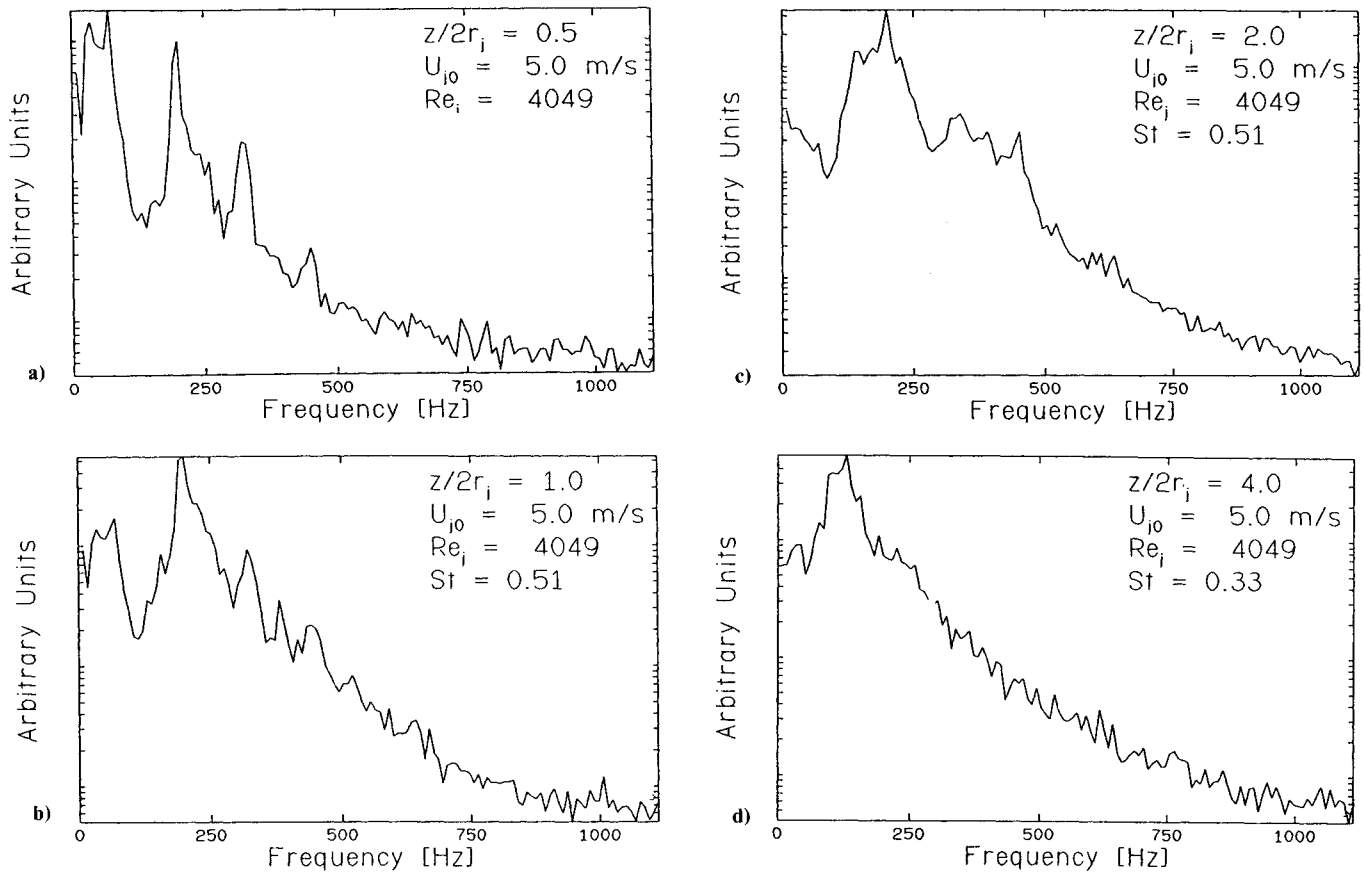

Fig. 14 Frequency spectra of centerline axial velocity for U_{jm} = 5.0 m/s: $z/(2r_j)$ = a) 0.5, b) 1.0, c) 2.0, and d) 4.0.

Farther downstream, lower frequencies get excited, and the energy associated with the 200 Hz decays. At $z/(2r_j) = 4$, the more energetic frequency is about 130 Hz, with the corresponding Strouhal number of 0.33. The aforementioned observations are in agreement with the work of Durao and Pita,[4] who reported the transition of the Strouhal number from 0.52-0.33, corresponding to the stations at 0.5 and 4 jet diam, respectively.

V. Conclusions

From the previous discussion, the following conclusions may be drawn:

1) The measurements show that the evolution of axial velocities, the separation size, and the near-wall behavior of the rms velocity were in excellent agreement with previous results.

2) The velocity spectra in the initial mixing zone demonstrate the existence of coherent structures. The Strouhal number range of 0.33-0.51 was in excellent agreement with previous work.

3) The limited previous measurements for separating conditions compared well with the present computations. The agreement was excellent for $Ct > 0.7$, where streamline curvature effects are minimal, and deteriorates with decreasing Ct number, mostly as a result of numerical diffusion.

4) Four variations of the k-ϵ model accounting for streamline curvature did not result in definitive improvement over the standard model, mainly due to the dominance of numerical diffusion.

5) The predictions using the present detailed inlet conditions satisfactorily agreed with measured profiles. The isotropic turbulence model, the numerical diffusion, and the presence of coherent structures are the main causes of disagreement.

Acknowledgments

This paper is based on the doctoral research of the first author at the University of Illinois at Urbana-Champaign. The calculations were carried out on a Cyber 175 computer at the University of Illinois. The authors are glad to acknowledge the financial support of the University of Illinois and DuPont Company.

References

[1]Barchilon, M. and Curtet, R., "Some Details of the Structure of an Axisymmetric Confined Jet with Backflow," *Journal of Basic Engineering,* Vol. 86, No. 4, 1964, pp. 777-787.

[2]Becker, H. A., Hottel, H. C., and Williams, G. C. (1962), "Mixing and Flow in Ducted Turbulent Streams," *Proceedings of the 9th Symposium (International) on Combustion,* The Combustion Inst., Pittsburgh, PA, 1962, pp. 7-20.

[3]de Vahl Davis, G. and Mallinson, G. D., "An Evaluation of Upwind and Central Difference Approximations by a Study of Recirculating Flow," *Computers and Fluids,* Vol. 4, No. 1, 1976, pp. 29-43.

[4]Durao, D. F. G. and Pita, G., "Coherent Structures in the Near Field of Round Jets," *Experiments in Fluids,* Vol. 2, No. 2, 1984, pp. 145-149.

[5]Durst, F. and Rastogi, A. K., "Turbulent Flow Over Two-Dimensional Fences," *Turbulent Shear Flows 2,* Springer-Verlag, Berlin, 1979, pp. 218-232.

[6]Hanjalic, K. and Launder, B. E., "Preferential Spectral Transport by Irrotational Straining," *Turbulent Boundary Layers,* American Society of Mechanical Engineers, New York, 1979, pp. 101-110.

[7]Kang, Y. and Suzuki, K., "Numerical Study of Confined Jets I. Prediction of Flow Pattern and Turbulence Quantities with a Two-Equation Model of Turbulence," *Memoirs of the Faculty of Engineering, Kyoto University,* Vol. XL, Pt. 2, 1978, pp. 41-61.

[8]Kang, Y. and Suzuki, K., "Numerical Study of Wall Heat Transfer in the Recirculating Flow Region of a Confined Jet," *Heat Trans-*

fer: Japanese Research, Vol. 11, No. 1, 1982, pp. 44–69.

[9]Khodadadi, J. M., "An Experimental and Numerical Investigation of Confined Coaxial Turbulent Jets," Ph.D. Thesis, Dept. of Mechanical and Industrial Engineering, Univ. of Illinois at Urbana-Champaign, 1986.

[10]Khodadadi, J. M., Nguyen, T. M., and Vlachos, N. S., "Laminar Forced Convective Heat Transfer in a Two-Dimensional 90° Bifurcation," *Numerical Heat Transfer,* Vol. 9, No. 6, 1986, pp. 677–695.

[11]Khodadadi, J. M. and Vlachos, N. S., "Computation of Confined Swirling Flows: Effects of Boundary Conditions and Turbulence Model," *Proceedings of the 5th International Conference on Numerical Methods in Laminar and Turbulent Flow,* Vol. I, Pineridge Press, UK, 1987, pp. 458–469.

[12]Kline, S. J. and McClintock, F. A., "Describing Uncertainties in Single-Sample Experiments," *Mechanical Engineering,* Vol. 75, No. 1, 1953, pp. 3–8.

[13]Laker, J. R., Verriopoulos, C. A., and Vlachos, N. S., "A Microprocessor Controlled Data Acquisition and Processing System for Hot-Wire Anemometry," *Proceedings of the 7th Biennial Symposium on Turbulence,* Univ. of Missouri-Rolla, 1981, pp. 120–128.

[14]Launder, B. E. and Spalding, D. B., "The Numerical Computation of Turbulent Flows," *Computer Methods in Applied Mechanics and Engineering,* Vol. 3, 1974, pp. 269–289.

[15]Leschziner, M. A. and Rodi, W., "Calculation of Annular and Twin Parallel Jets Using Various Discretization Schemes and Turbulence-Model Variations," *Journal of Fluids Engineering,* Vol. 103, No. 2, 1981, pp. 352–360.

[16]Patankar, S. V., *Numerical Heat Transfer and Fluid Flow,* Hemisphere, New York, 1980.

[17]Razinsky, E. and Brighton, J. A., "Confined Jet Mixing for Nonseparating Conditions," *Journal of Basic Engineering,* Vol. 93, No. 3, 1971, pp. 333–349.

[18]Suzuki, K., Ida, S., and Sato, T., "Turbulence Measurements Related to Heat Transfer in an Axisymmetric Confined Jet with Laser Doppler Anemometer," *Proceedings of the 4th International Symposium on Turbulent Shear Flows,* Univ. of Karlsruhe, FRG, Paper 18.1–18.6, 1983.

[19]Vlachos, N. S., "LDA Measurements of Natural Transition in a Confined Round Jet," *Proceedings of the 8th Biennial Symposium on Turbulence,* Univ. of Missouri-Rolla, Paper 10.1–10.8, 1983.